PHYSICAL REVIEW E **80**, 016409 (2009)

Interaction of an ultrashort laser pulse and relativistic electron beam in a corrugated plasma channel

J. P. Palastro
Lawrence Livermore National Laboratory, Livermore, California 94551, USA

T. M. Antonsen
Institute for Research in Electronics and Applied Physics, University of Maryland, College Park, Maryland 20742, USA

(Received 25 August 2008; revised manuscript received 8 May 2009; published 28 July 2009)

Copropagation of a laser pulse and a relativistic electron beam in a corrugated plasma channel has been proposed for the direct laser acceleration of electrons [Palastro *et al.*, Phys. Rev. E **77**, 036405 (2008)]. The corrugated plasma channel allows for the guiding of laser pulses composed of subluminal spatial harmonics. Phase matching between the electron beam and the spatial harmonics results in acceleration, but for high beam densities, the pulse energy can be rapidly depleted. This depletion may result in interaction times shorter than the waveguide length limited time or pulse length dephasing time. We present an analytic model and self-consistent simulations of the electron beam–laser pulse interaction. A linear dispersion relation is derived. The effect of the electron beam on the pulse after the occurrence of axial bunching is examined. Injection of axially modulated electron beams is also explored. In particular, we find that a properly phased electron beam can transfer energy to the laser pulse as an inverse process to acceleration.

DOI: 10.1103/PhysRevE.80.016409 PACS number(s): 52.38.Kd, 41.75.Jv, 41.75.Fr

I. INTRODUCTION

Advancements in laser technology have resulted in ever shorter and more energetic laser pulses. The relative ease of generating energetic laser pulses at near-optical frequencies has spawned an entire field—laser-matter interactions—the goal of which is the efficient coupling of laser energy into matter. Typically, the matter is used to drive a secondary process inaccessible to solid-state technology: x-ray sources for indirect inertial confinement fusion or backlighting [1,2], the creation of hot spots in fast ignition targets [3], noninvasive cancer therapy [4], nuclear stimulation [5], and the creation of nonlinear plasma wakefields [6]. Perhaps the most rapidly expanding and widely accessible subfield of laser-matter interactions is laser-based electron acceleration.

Several schemes have been proposed or demonstrated for electron acceleration [6–11] with laser-wakefield acceleration providing the largest energy gains to date: Leemans *et al.* observed gradients of ~500 MeV/cm, 3 orders of magnitude higher than the Stanford Linear Accelerator, but only over ~2 cm [7]. Wakefield acceleration, by design, relies on the nonlinear ponderomotive force of the laser to drive large amplitude plasma waves and, as a result, requires high-power short-pulse lasers. Several methods for the direct laser acceleration of electrons have been proposed as lower laser power alternatives to wakefield acceleration, including the semi-infinite vacuum accelerator [10], the inverse Cherenkov accelerator [11], and the axially uniform plasma channel accelerator [12]. For all of these schemes, however, the maximum energy gain of electrons is much lower than those achieved in wakefield accelerators.

Direct laser acceleration of electrons in corrugated plasma channels [13,14] utilizes the linear laser electric field and as a result requires lower pulse powers (<1 TW) at low pulse energies (~300 mJ), while still providing reasonable gradients ~100 MeV/cm. Creation of the corrugated plasma channel has been demonstrated [15] and potential creation mechanisms were proposed [16]. If the channel and laser parameters are chosen properly, a guided radially polarized short-pulse laser can transfer energy to a relativistic electron beam through quasi-phase-matched acceleration (QPMA). The radial polarization of the laser provides an axial electric field component necessary for acceleration. The axially periodic structure of the channel provides a phase modulation of the laser, resulting in oscillations of the laser phase velocity. The electrons are more closely phase matched to the laser when the axial field strength is high and out of phase with the laser when the axial field strength is low—quasiphase matching. The same phenomenon can be interpreted as the guided mode being composed of subluminal spatial harmonics: one of these harmonics can be phase matched to the relativistic electron beam, providing linear energy gain over long distances.

A scaling law for the energy gain of QPMA in corrugated plasma channels predicts much higher energy gains than other direct acceleration schemes and compares favorably to wakefield acceleration at low pulse energies [13,14]. For a laser pulse with a duration of 300 fs, spot size of 15 μm, and normalized vector potential of $a_0 = 0.25$, matched to plasma channel with an on-axis electron density of $7 \times 10^{18}/\text{cm}^{-3}$, corrugation size of 350 μm, and a relative modulation amplitude of 0.9, the scaling law predicts an energy gain of several hundred MeV for an initial electron-beam energy of 50 MeV. Similar scaling laws using the same parameters for semi-infinite vacuum acceleration predict energy gain of tens of MeV, while scaling laws for resonant wakefield acceleration predict several hundred MeV (the pulse length is shortened to match the plasma length but the laser amplitude increased to maintain the pulse energy). All of the parameters used are experimentally realizable and clearly demarcate the parameter region of interest for QPMA in corrugated plasma channels.

In addition to axial acceleration, the guided mode also provides focusing forces that confine high-energy electrons on axis, while expelling low-energy electrons from the center of the beam. Half of the electrons in the accelerating phase are initially focused while the other half defocused. If the channel and beam parameters are chosen properly, there is a maximum phase slip for the accelerated electrons. Initially accelerated and focused electrons can remain in the focusing/acceleration phase indefinitely, creating a well-collimated, high-energy bunch. Spatial filtering of the electron beam could then be used remove the high divergence (low axial momentum) portion of the beam, leaving the high axial momentum, low divergence subset.

Our previous studies have demonstrated the phenomenon of quasiphase matching, verified the scaling law, and examined the transverse beam dynamics. The beam-pulse interaction, however, was not handled self-consistently. Here we consider the self-consistent interaction of the laser pulse and electron beam in order to study the effects of energy transfer. Our previous scaling laws assumed the acceleration distance was limited by "pulse length dephasing"—the time it takes for the electrons to outrun the laser pulse. If the pulse energy, and concomitantly the field amplitude, cannot be sustained over this distance, the energy gains could be significantly lower. An examination of the self-consistent beam-pulse interaction is thus a necessity for understanding the limitations of QPMA in corrugated plasma channels.

This paper is organized as follows. In Sec. II, we present our model of laser-pulse propagation that separates the transverse equation determining the evolution of the laser phase and the equation determining the evolution of the longitudinal pulse shape. Section III presents the linear dispersion relation for the interaction of the short-pulse laser and relativistic electron beam. In Sec. IV, we briefly discuss the reaction of the channel to the electron beam driven wakefields. Section V contains our numerical algorithm of the pulse-beam interaction and analysis of our simulation results. Section VI discusses the inverse process by which a properly phased electron beam can transfer energy to the short-pulse laser. Section VII includes our summary and conclusions.

II. LASER-PULSE PROPAGATION MODEL

We start with Maxwell's equations for the electromagnetic field in the presence of a background plasma and electron-beam current

$$\nabla \times \vec{E} = -\frac{1}{c}\frac{\partial \vec{B}}{\partial t}, \tag{1}$$

$$\nabla \times \vec{B} = \frac{1}{c}\frac{\partial \vec{D}}{\partial t} + \frac{4\pi}{c}\vec{J}_b, \tag{2}$$

where $\vec{J}_b$ is the relativistic beam current, $\hat{\vec{D}}(\omega) = \varepsilon(r,z,\omega)\hat{\vec{E}}(\omega)$, the carrot notation represents a temporally Fourier-transformed variable, and $\varepsilon(r,z,\omega)$ is the dielectric constant for the background plasma. Following Ref. [13], we consider a cold, nonrelativistic background plasma with a dielectric constant given by $\varepsilon(r,z,\omega) = 1-\omega_p^2(r,z)/\omega^2$, where $\omega_p^2 = 4\pi e^2 n_e(r,z)/m_e$, e is the electron charge, m_e the electron mass, and $n_e(r,z)$ is the electron density. The electron-density profile is meant to model the experimentally produced corrugated plasma waveguides [15], paralleling our previous studies [13]

$$n_e(r,z) = n_o[1+\delta \sin(k_m z)] + n_o'' r^2/2, \tag{3}$$

where δ is the relative amplitude of the density modulation, n_o'' determines the radial dependence, and k_m is the wave number describing the axial periodicity of the channel.

The electromagnetic field is expressed as

$$\vec{E}(\vec{x},t) = \eta(z,t)\vec{\xi}(\vec{x})e^{i(k_0 z-\omega t)} + \text{c.c.}, \tag{4}$$

$$\vec{B}(\vec{x},t) = \eta(z,t)\vec{\beta}(\vec{x})e^{i(k_0 z-\omega t)} + \text{c.c.}, \tag{5}$$

where k_o and ω are the central wave number and frequency of the laser pulse, respectively, $\vec{\xi}$ and $\vec{\beta}$ are the envelopes determining the transverse structure, amplitude, and phase of the field, and $\eta(z,t)$ is a "superenvelope" determining the longitudinal pulse shape. In particular, $\vec{\xi}$ and $\vec{\beta}$ respond to the background plasma and $\eta(z,t)$ responds to the relativistic electron beam. We are interested in radially polarized modes, $\vec{\xi} = (\xi_r, 0, \xi_z)$ and $\vec{\beta} = (0, \beta_\theta, 0)$, which provide the axial field component necessary for acceleration of the electron beam. We assume that the pulse remains azimuthally symmetric for all time and consider corrugated plasma channels paralleling those created by Layer *et al.* [15] for which the plasma frequency satisfies $\omega_p \ll \omega$. As discussed in Appendix A, the equations for $\vec{\xi}$ and $\eta(z,t)$ can be separated with ξ_r satisfying

$$\left[2ik_o\frac{\partial}{\partial z} + \frac{1}{r}\frac{\partial}{\partial r}r\frac{\partial}{\partial r} - \frac{1}{r^2}\right]\xi_r = \frac{\omega_p^2(r,z)}{c^2}\xi_r. \tag{6}$$

In our previous work, it was shown that the lowest radial eigenmode solution to this equation for the density profile in Eq. (3) is

$$\xi_r(r,z) = \xi_0\frac{r}{w_{ch}}e^{-r^2/w_{ch}^2}\sum_m i^m J_m(\psi)e^{-i\psi+i(\delta k+mk_m)z}, \tag{7}$$

where $w_{ch} = (2c)^{1/2}(2/\omega_{p,0}''^2)^{1/4}$ is the matched spot size of the plasma channel, $\delta k = -k_0[\omega_p^2/2\omega^2 + 4/(k_0 w_{ch})^2]$ is the wave-number shift due to the background plasma and channel, and $\psi = \delta\omega_{p,0}^2/2c^2 k_0 k_m$ is the amplitude of the periodic phase modulation from the modulated density profile. With Eq. (7), ξ_z and β_θ can be found via Eqs. (1) and (2),

$$(\nabla + ik_0\hat{z}) \times \vec{\xi} = \frac{i\omega}{c}\vec{\beta}, \tag{8}$$

$$(\nabla + ik_0\hat{z}) \times \vec{\beta} = -\frac{i\omega}{c}\varepsilon\vec{\xi}, \tag{9}$$

where $d/dz \ll k_0$ is understood in Eqs. (8) and (9).

The equation for the superenvelope $\eta(z,t)$ is obtained by forming the dot product of Eq. (2) with the conjugate of the eigenmode, Eq. (7), and using Eq. (1). This is made rigorous by a first-principles approach found in Appendix A which shows that the equations describing the evolution of $\vec{\xi}$, Eq. (6), and $\eta(z,t)$ can be separated with $\eta(z,t)$ satisfying

$$\left[\frac{\partial}{\partial z}+\frac{1}{c_g}\frac{\partial}{\partial t}\right]\eta(z,t)=-\frac{2\pi}{cP}\int\vec{\xi}^{*}(r,z)\cdot\vec{J}_b(r,z,t)e^{-i(k_o z-\omega t)}d^2r, \tag{10}$$

where P is the power flow given by Eq. (A17) and $c_g=1-\omega_p^2/2\omega^2-4/(k_o w_{ch})^2$ is the group velocity. The integral represents the energy transfer per unit length between the laser pulse and electron beam. For low beam currents, the integral can be neglected and the solution reduces to $\eta(z,t)=\eta(z-c_g t)$. This situation has been examined previously with η chosen as a Gaussian pulse. Inclusion of this integral allows for the self-consistent treatment of energy transfer, beam evolution, and laser propagation.

III. LINEAR DISPERSION RELATION FOR $\eta(z,t)$

We consider linear perturbations on a relativistic, axially uniform electron beam with an arbitrary radial profile copropagating with a laser pulse. The expressions for the density and flow velocity are

$$n_b=n_{b,o}(r)+n_{b,1}(r,z,t), \tag{11}$$

$$\vec{u}_b=v_{z,o}\hat{z}+\vec{u}_1(r,z,t). \tag{12}$$

The spatiotemporal dependence of the first-order quantities arises from the beam's electromagnetic response to the laser pulse. Linearizing the relativistic factor, γ, we have

$$\gamma=\gamma_0\left(1+\gamma_0^2\frac{v_{z,0}u_{z,1}}{c^2}\right), \tag{13}$$

where $\gamma_0=(1-v_{z,0}^2/c^2)^{-1/2}$. We can now find three equations for the first-order quantities n_1, $u_{1,r}$, and $u_{1,z}$ in terms of the equilibrium quantities and laser electromagnetic field.

We note that the laser field driving the electron beam consists of a superposition of waves with wave numbers $\hat{k}_m=k+mk_m$, where $k=\delta k_\eta+\delta k+k_0$, δk_η is the wave number associated with the superenvelope, δk is the wave-number shift due to the average plasma channel defined after Eq. (7), $k_0=\omega/c$, and k_m is the modulation wave number (in this context, the subscript m refers to modulation and not the summation variable). Thus, the perturbed beam quantities will also be superpositions of waves with the same wave numbers, $n_{b,1}=\Sigma_m n_m\exp[i(\hat{k}_n z-\omega t)]$ and $\vec{u}_{b,1}=\Sigma_m\vec{u}_m\exp[i(\hat{k}_m z-\omega t)]$. Which of these amplitudes is important will depend on the size of the channel density modulation and the value of the Doppler-shifted frequency, $\omega-\hat{k}_m v_{z0}$. The linearized equations of continuity and momentum balance then give us for each wave number

$$-i(\omega-\hat{k}_m v_{z0})n_m=-\left[\frac{\partial}{r\,\partial r}(rn_{b,0}u_{r,m})+i\hat{k}_m n_{b,0}u_{z,m}\right], \tag{14}$$

$$-i(\omega-\hat{k}_m v_{z0})u_{z,m}=\frac{q}{m\gamma_0^3}E_{z,m}, \tag{15}$$

$$-i(\omega-\hat{k}_m v_{z0})u_{r,m}=\frac{q}{m\gamma_0}\left(E_{z,m}-\frac{v_{z0}}{c}B_{\theta,m}\right), \tag{16}$$

where from Eq. (1) we have

$$B_{\theta,m}=\frac{\hat{k}_m c}{\omega}E_{r,m}+\frac{ic}{\omega}\frac{\partial}{\partial r}E_{z,m} \tag{17}$$

and $E_{z,m}$ and $E_{r,m}$ are the amplitudes of the different spatial harmonics implied by Eq. (7).

The perturbed current density to be inserted in Eq. (10) can be expressed in terms for the perturbed beam quantities as

$$\vec{J}_{b,1}=q\sum_m(n_{b,0}\vec{u}_m+n_m\vec{z}v_{z0})\exp[i(\hat{k}_m z-\omega t)]. \tag{18}$$

The fluid equations (14)–(16) can be solved to express the perturbed current density (18) in terms of the superenvelope η and the profiles for the radial and axial components of the mode field, which are common to each spatial harmonic,

$$u_r=\frac{r}{w_{ch}}\exp\left(-\frac{r^2}{w_{ch}^2}\right), \tag{19a}$$

and

$$u_z=\frac{2c}{\omega w_{ch}}\left(1-\frac{r^2}{w_{ch}^2}\right)\exp\left(-\frac{r^2}{w_{ch}^2}\right). \tag{19b}$$

Inserting these quantities into the wave equation (10) for the superenvelope and selecting the component with spatial wave number k results in the dispersion relation,

$$c\left[k-\left(\frac{\omega}{c}+\delta k+\delta k_b\right)\right]+\sum_m\left(\frac{\omega_{MT,m}^2}{[\omega-(k+mk_m)v_{z0}]}+\frac{\omega_{OT,m}^3}{[\omega-(k+mk_m)v_{z0}]^2}\right)=0, \tag{20}$$

where

$$\delta k_b=-\left\langle\frac{\omega_b^2(r)}{2\omega c\gamma_0}u_r^2\right\rangle, \tag{21a}$$

$$\omega_{MT,m}^2=J_m^2(\psi)\left\langle\frac{\omega_b^2(r)}{\gamma_0}u_r\frac{v_{z,0}}{\omega}\frac{\partial u_z}{\partial r}\right\rangle, \tag{21b}$$

and

$$\omega_{OT,m}^3=J_m^2(\psi)\left\langle\frac{\omega\omega_b^2(r)}{2\gamma_0}\left[\frac{u_z^2}{\gamma_0^2}+\left|\frac{v_{z0}}{\omega}\frac{du_z}{dr}\right|^2\right]\right\rangle. \tag{21c}$$

Here we have defined the beam plasma frequency, $\omega_b^2(r)=4\pi q^2 n_{b,0}(r)/m_e$, and an angular bracket around a function f is defined as $\langle f\rangle\equiv\int d^2rf/\int d^2ru_r^2$ where the integral is taken over all r. The three terms described by Eqs. (21a)–(21c) represent the response of the beam. The first term, Eq. (21a), represents the wave-number shift due to the radial polarizability of the electron beam. Note that it is in the same form as the wave-number shift defined after Eq. (7). The second and third terms, which appear over resonant denominators, describe the bunching of the beam and represent a possible source of resonant energy exchange between the beam and the wave. The term $\omega_{OT,m}^3$ given by Eq. (21c) is a result of the perturbed axial current and consists of two contributions. One is proportional to u_z^2/γ_0^3, which represents the effect of axial bunching of the beam. This form of bunching is referred to at O-type bunching in the vacuum electronics literature [17]. The second contribution to Eq. (21c) is proportional to $(du_z/dr)^2/\gamma_0$ and represents a contribution to the perturbed density from the divergence of the portion of the radial velocity due to the perturbed magnetic field. (This term is responsible for the Weibel instability in an anisotropic plasma.) Which of the two contributions to Eq. (21c) dominates depends on the width of the electron beam and the value of its relativistic factor. If the beam is so narrow that all particles can be considered to be on axis, then first term representing O-type bunching dominates. On the other hand, if the beam energy is very high, then it is hard to bunch the beam and the second term dominates. The term given by Eq. (21b) enters the dispersion relation in the numerator of a fraction whose denominator is a single power of the Doppler-shifted frequency as opposed to the case of the term (21c) where the Doppler-shifted frequency is squared. This is known as M-type bunching in the vacuum electronics community. It results from the beam electrons being laterally deflected in the presence of an inhomogeneous axial electric field. For the case of a very narrow electron beam, this term is zero. Note that although we have written Eq. (21b) as the square of a frequency, actually its sign is undetermined. In our analysis, we have assumed that the dominant field components present are those associated with the electromagnetic mode of the channel. Thus, we have neglected the space-charge fields, which are proportional to the beam density and that are not part of the electromagnetic mode of the modulated plasma channel. Inclusion of these fields will modify the denominators in Eq. (20). For example, the denominator of the O-type term becomes $[\omega-(k+mk_m)v_{z0}]^2-R\omega_b^2/\gamma_0^3$, where ω_b^2 represents an average of the beam plasma frequency and $R<1$ is the space-charge reduction factor [18] due to the fact that space-charge fields are distributed outside the beam. The space-charge fields can be negligible if the Doppler-shifted frequency is large enough.

To analyze the dispersion relation, we refer all frequencies to the Doppler-shifted beam frequency for the $m=1$ spatial harmonic. Further, we keep only the $m=1$ terms in the sum on spatial harmonics (this is valid if the electron-beam velocity is nearly matched to the phase velocity of the $m=1$ spatial harmonic) and we neglect the M-type bunching term assuming the beam to be narrow. The result is a cubic dispersion relation for the Doppler-shifted frequency, $\Omega=\omega-(k+k_m)v_{z0}$,

$$[\Omega^2-R\omega_b^2/\gamma_0^3](\Omega-\Delta\Omega)-\omega_{OT,1}^3=0, \tag{22}$$

where $\Delta\Omega=c(k-\delta k-\delta k_b)-(k+k_m)v_{z0}$ is the frequency difference between the electromagnetic mode $c(k-\delta k-\delta k_b)$ and the beam Doppler frequency shift $(k+k_m)v_{z0}$. In this case, the dispersion relation (22) reduces to the standard Pierce-type [19] dispersion relation.

Correspondence to the Pierce dispersion relation is made clear by considering the ratio of the growth rate to the wave frequency, defined as the Pierce parameter C, given in Ref. [19]

$$\frac{\omega_{OT,m}^3}{\omega^3}\equiv C^3=\frac{2\pi I}{I_A\beta_0\gamma_0^3}\left(\frac{K}{377\ \ \Omega}\right), \tag{23}$$

where $\beta_0=v_{z0}/c$, we assume $\omega\cong kc$, $I_A=m_ec^3/q$, which has a value of 1.7×10^4 A when expressed in SI, and Ω in Eq. (23) refers to Ohms. The quantity K is known as the coupling impedance and is defined in SI as

$$K=\frac{|E_{z,1}(0)|^2}{2k^2P}, \tag{24}$$

where P is the power in the wave and $|E_{z,1}(0)|$ is the on-axis, axial electric field magnitude of the resonant spatial harmonic. The coupling impedance here is defined for the case of a narrow beam where only the first contribution to $\omega_{OT,1}$ in Eq. (21c) is important. In terms of the field structure defined in Eq. (19), the impedance is given by

$$\frac{K}{377\ \ \Omega}=\frac{J_1^2(\psi)|u_z(0)|^2}{k^2\int_0^\infty 2\pi r dr u_r^2}. \tag{25}$$

The effect of space charge is characterized by the parameter Q defined as follows:

$$\frac{R\omega_b^2}{k^2c^2\gamma_0^3}\equiv 4QC^3. \tag{26}$$

The solutions of the dispersion relation (22) depend on the frequency shift $\Delta\Omega$, the O-Type bunching frequency $\omega_{OT,1}$, and the beam space-charge frequency, $\sqrt{R\omega_b^2/\gamma_0^3}$. Two regimes are of interest—strong and weak space charges. In the case of weak space charge $R\omega_b^2/\gamma_0^3\ll\omega_{OT,1}^2$, the maximum growth occurs for zero-frequency shift and the three solutions are given by

$$\Omega=\omega_{OT,1}[1,\ e^{i2\pi/3},\ e^{-i2\pi/3}]. \tag{27}$$

Of these, the middle one is unstable, with a growth rate $\mathrm{Im}(\Omega)=\sqrt{3}\omega_{OT,1}/2$ and a frequency $\mathrm{Re}(\Omega)=-\omega_{OT,1}/2$. The negative sign to the Doppler shifted frequency indicates that the beam speed is slightly greater than the phase velocity of the wave being amplified. This is consistent with the picture of the instability as a process in which the beam speed is lowered to the phase velocity of the wave as energy is transferred from the beam to the wave and the wave grows. The range of frequency shifts for which the waves are unstable can be determined in the weak space-charge case to be $\Delta\Omega>-3\omega_{OT,1}/2^{2/3}$. The dependence of the frequency shift on wave number is similar to that of a free-electron laser. In particular, there will be either two wave numbers giving zero-frequency shift or none. These wave numbers correspond to points where the dispersion curves for the beam mode and electromagnetic mode cross in the ω vs k plane. The intersection points may be found from the quadratic equation

$$\Delta\Omega(k) = ck + \frac{\omega_c^2}{2ck} - (k + k_m)v_{z0} = 0, \tag{28}$$

where $\omega_c^2 = \omega_{p0}^2 + 8c^2/w_{ch}^2 + \langle \omega_b^2 u_r^2/\gamma_0 \rangle$ is the square of the effective cutoff frequency for the electromagnetic mode including contributions from the plasma, the channel, and the beam. In Eq. (28), we have replaced ω by ck in the definitions of the wave-number shifts δk, δk_b appearing in Eq. (22). This applies for frequencies well above the cutoff frequency. Solving for the intersection points, we have $\Delta\Omega(k_\pm) = 0$, where

$$k_\pm = \frac{k_m \beta_0}{2(1-\beta_0)}\left[1 \pm \sqrt{1 - \frac{4\omega_c^2(1-\beta_0)}{(k_m c \beta_0)^2}}\right]. \tag{29}$$

There are no intersection points in cases in which the radical is imaginary.

In the case of strong space charge $R\omega_b^2/\gamma_0^3 \gg \omega_{OT,1}^2$, the maximum growth occurs when the frequency shift coincides with the slow space-charge wave, $\Delta\Omega = -\sqrt{R\omega_b^2/\gamma_0^3}$. In this case, the dispersion relation can be approximated as

$$-2\sqrt{R\omega_b^2/\gamma_0^3}\left[\Omega + \sqrt{R\omega_b^2/\gamma_0^3}\right](\Omega - \Delta\Omega) - \omega_{OT,1}^3 = 0. \tag{30}$$

Thus, two of the three solutions of Eq. (22) are described by

$$\Omega = -\sqrt{R\omega_b^2/\gamma_0^3} \pm i\left[(\omega_{OT,1}^3/2)/\sqrt{R\omega_b^2/\gamma_0^3}\right]^{1/2}. \tag{31}$$

The third solution in this case is a stable beam plasma oscillation $\Omega = \sqrt{R\omega_b^2/\gamma_0^3}$. In the strong space-charge case, instability is present only for a range of wave numbers satisfying $|\Delta\Omega(k) + \sqrt{R\omega_b^2/\gamma_0^3}| < [2\omega_{OT,1}^3/\sqrt{R\omega_b^2/\gamma_0^3}]^{1/2}$.

We consider the following parameters: matched beam width of $w_{ch} = 15$ μm, on-axis plasma density $n_o = 7 \times 10^{18}$ cm^{-3}, corrugation amplitude $\delta = 0.9$, and a modulation period of $T_m = 0.035$ cm. For these, the lower intersection given by Eq. (25) corresponds to a vacuum wavelength $\lambda = 800$ nm. Calculation of the impedance results in $K = 1.53 \times 10^{-6}$ Ω. We then consider two different beam densities: $n_b = 3 \times 10^{16}$ and 3×10^{18} cm^{-3}. The beam radius, σ_b, is taken to be 1 μm and beam energy corresponding to $\gamma_0 = 100$. The two values of beam current are then 4.5 and 4.5×10^2 A. The values of the beam plasma frequency $\omega_Q = \sqrt{R\omega_b^2/\gamma_0^3}$ in the two cases are 9.8×10^9 and 9.8×10^{10} s^{-1} (here we assume $R = 1$). The values of $\omega_{OT,1}$ in the two cases are 4.3×10^9 and 2×10^{10} s^{-1}. Thus, the strong space-charge result is more appropriate, although the lower density is near the boundary separating the strong and weak space-charge regimes. Using the strong space-charge formula, we arrive at growth rates of 1.0×10^9 and 6.4×10^9 s^{-1}, respectively, in the two cases. These growth rates correspond to growth lengths of 15.0 and 4.7 cm, which are longer than existing channels, (1.5 cm) but not by a large factor.

The analysis above provides a basic understanding of the linear electron beam–laser pulse interaction. The time scale for an initially unmodulated beam, in the presence of a weak injected radiation pulse, to develop modulations at the radiation frequency is the inverse of the growth rate given by either Eq. (27) or (31). As the modulations grow, energy is extracted from the beam, the beam slows down, and the radiation pulse amplitude grows. The process saturates when the beam velocity moves out of resonance with the wave. The change in beam speed δv_z accompanying the saturation process can be estimated from the growth rate as $(k + k_m)\delta v_z = \mathrm{Im}(\Omega)$. At this point, the beam will have transferred an amount of power

$$P_S \cong (I/q)\frac{m_e \gamma_0^3 v_{z0}\,\mathrm{Im}(\Omega)}{k}, \tag{32}$$

where I is the beam current and we have assumed $k \gg k_m$. This power level defines a reference level for cases in which the beam interacts with an injected laser pulse. If the injected laser-pulse power is below the level P_S, then modulation of the beam will occur on the linear time scale. If the injected pulse power is above the level P_S, then the laser electric field amplitude can be considered constant during the modulation process. We calculate from Eq. (31) $P_s = 2.0 \times 10^6$ and 6.3×10^8 W in the two cases under consideration.

We note that if the injected power is high enough space-charge fields at the laser frequency can be neglected completely. The axial field of the laser pulse will cause the beam to bunch in a characteristic time τ_{NL} given by

$$\tau_{NL}^{-2} = \frac{qk|E_{z,1}|}{m\gamma_0^3} = \frac{qk^2\sqrt{2KP}}{m\gamma_0^3}. \tag{33}$$

If this bunching time is shorter than the beam plasma frequency, then space-charge debunching will be overcome by the laser field. We find that this is the case if $P > 1.0 \times 10^{11}$ or $P > 1.0 \times 10^{12}$ W in the two example cases. For the parameters that we consider in the remainder of the paper, $P \cong 1 \times 10^{12}$. We will assume that the quasi-phase-matched axial component of the laser field is strong enough to dominate the debunching space-charge fields.

IV. BEAM DRIVEN WAKEFIELDS IN QUASI-PHASE-MATCHED ACCELERATION

The space-charge forces of the beam can also drive wakefields in the background plasma channel. For narrow beams considered here (the beam does not experience the transverse variation in the plasma channel) and noting that $k_m \ll k_p$, the channel appears spatially uniform to the beam. Su *et al.* [20] and others [21,22] provided expressions for the wakefields generated by quadratic beams in uniform channels. For a beam density profile $n_b(r) = n_{b,0}(1 - r^2/\sigma_b^2)$ for $r \leq \sigma_b$ and zero otherwise, the wakefields are

$$E_z = 8\pi q n_{b,0}\left[K_2(k_p\sigma_b)I_0(k_p r) + \frac{1}{2}\left(1 - \frac{r^2}{\sigma_b^2}\right) - \frac{2}{(k_p\sigma_b)^2}\right] \times \int_0^\zeta d\zeta' f(\zeta')\cos[k_p(\zeta - \zeta')], \tag{34}$$

$$E_\perp = 8\pi q n_{b,0}\left[K_2(k_p\sigma_b)I_1(k_p r) - \frac{r}{k_p\sigma_b^2}\right] \times\int_0^{\zeta} d\zeta' f(\zeta')\sin[k_p(\zeta-\zeta')]. \tag{35}$$

With the expressions above, we can approximate the magnitude of the electric field due to a Gaussian beam profile. For a uniform beams with σ_b on the order of the plasma wavelength, we can approximate the maximum fields (which occur at different radii for the axial and transverse fields) as follows: $qE_z/mc\omega_p \cong (2\mu_z/\pi)r_e\lambda_p^2 n_{b,0}$ and $qE_\perp/mc\omega_p \cong (2\mu_\perp/\pi)r_e\lambda_p^2 n_{b,0}$, where r_e is the classical electron radius and μ_z and $\mu_\perp$ are numerical factors of order 1. For a channel density of 7×10^{18} cm^{-3} and beam density of 1×10^{18} cm^{-3}, we find $qE/mc\omega_p \sim 3\times10^{-4}$, which suggests that ignoring the reaction of the channel to the beam is reasonable. We now focus on the effect of depletion of the laser field due to acceleration of the electron beam.

V. SELF-CONSISTENT SIMULATION OF BEAM-PULSE INTERACTION

For simulating the interaction of a relativistic beam with the short-pulse laser, we numerically solve Eq. (6) for the density profile in Eq. (3) from $z=-20R_L$ to $20R_L$, where R_L is the Rayleigh length defined as $R_L=\pi w_{ch}^2/\lambda_0$ ($20R_L$ is the physical length of the corrugated plasma channel $\sim$1.8 cm). Because the radial solutions of Eq. (6) are known to be $2^{-\ell}H_{2n+1}(r/w_{ch})e^{-r^2/w_{ch}^2}$, where H_n is the nth Hermite polynomial, Eq. (6) only needs to be integrated axially and ξ_r grided axially. Here we only consider propagation of the lowest radial eigenmode (this simplification is discussed further in Appendix B). For the density profile considered here, Eq. (3), an analytic solution for the axial dependence exists, Eq. (7), but the simulation is written to handle arbitrary axial dependence of the plasma density. The channel and laser parameters are the same used in our analysis of the linear dispersion relation, which has the phase velocity of the $n=1$ spatial harmonic set to c.

The pulse is initiated as a Gaussian with temporal width σ_t centered about $z=0$ with a full width half maximum of $[4\sigma_t^2 \log_e(2)]^{1/2}=500$ fs. The electron beam is initiated as an axially uniform beam extending from $z=-3c\sigma_t$ to $3c\sigma_t$ with a Gaussian radial profile of width σ_b. Each electron starts with an energy of $\gamma_0=100$. To reduce numerical noise, the simulation particles are initially placed with uniform axial separation and Gaussian separation in radius. Gaussian radial separation entails placing the nth particle at the radii, r_n, defined as follows:

$$\int_0^{r_n} e^{-r^2/\sigma_b^2}d^2r = \pi\sigma_b^2\left(\frac{n}{N_r}\right), \tag{36}$$

where N_r is the number of radial positions. For the parameters considered here, 10^4 axial positions and $N_r=10$ are sufficient to eliminate particle noise ($N_{sim}=10^5$ total simulation particles).

At each time step, the three-dimensional electron equations of motion are solved for the position $\vec{x}$ and momentum $\vec{p}$,

$$\frac{d\vec{p}}{dt} = 2q\,\mathrm{Re}\left[\eta(z,t)e^{i(k_0z-\omega t)}\left(\vec{\xi}(r,z) + \frac{\vec{p}}{\gamma m_e}\times\vec{\beta}(r,z)\right)\right], \tag{37}$$

$$\frac{d\vec{x}}{dt} = \frac{\vec{p}}{\gamma m_e}. \tag{38}$$

The phase, $(k_0z-\omega t)$, is evaluated explicitly. The spatial phase is well resolved; there are $\sim$15 simulation particles per laser wavelength. The temporal phase, ωt, is not resolved by the time step, but the effective temporal phase, $(\omega - v_{z0}k_0)t$, is well resolved. With the generalized coordinates, the current density can be calculated

$$\vec{J}_b(r,z,t) = \frac{q\varpi}{2\pi m_e}\sum_{part.}\frac{\vec{p}_i(t)}{\gamma_i(t)r_i(t)}\delta[r-r_i(t)]\delta[z-z_i(t)], \tag{39}$$

where $\varpi = \int n_b(r,z,t)d^2r/N_{sim}$ converts the simulated beam density to the appropriate physical density. Inserting Eq. (39) into Eq. (10), we find

$$\left[\frac{\partial}{\partial z} + \frac{1}{c_g}\frac{\partial}{\partial t}\right]\eta = -\frac{2\pi q\varpi}{cP}e^{i\omega t}\sum_{part.}\vec{\xi}^*(r_i,z_i)\vec{v}_i(t)e^{-ik_0z_i}. \tag{40}$$

Because we have already grided $\vec{\xi}$ axially and we know the radial dependence, the current density is never placed on a numerical grid for calculating the right-hand side of Eq. (40). This property reduces both the noise and computation time of the simulation. With the current source determined, Eq. (40) is solved in a window traveling at c_g that extends $-10c\sigma_t$ to $10c\sigma_t$ about the center of the pulse. At each time step, the process is repeated with the time step, Δt, chosen to satisfy the Courant condition of $\Delta z/c\Delta t \sim 3/4$ for a chosen spatial step, Δz.

We consider two densities $n_b=3\times10^{16}$ cm^{-3} and 3×10^{18} cm^{-3}, which we propagate over 3.6 cm, twice the channel length corresponding to Ref. [15]. As discussed in Sec. II, this distance is shorter than the distance required for linear space-charge instabilities develop, which cannot be examined with our self-consistent simulation. We also note that 3.6 cm is about the pulse length dephasing length (there cannot be pump depletion if the electron beam and laser pulse do not overlap). For each beam density, we consider two beam widths: $\sigma_b=1$ μm and $\sigma_b=3$ μm, corresponding to total beam charges of $\sim$26 and 230 pC for $n_b=3\times10^{16}$ cm^{-3} and $\sim$2.6 and 23 nC for $n_b=3\times10^{18}$ cm^{-3}, respectively.

Figure 1 shows the pulse evolution in a frame moving at c_g our four cases. For both beam widths pump depletion was negligible until the total beam charge exceeded 10 nC; there is visible narrowing and drop in the envelope's amplitude for the 23 nC beam. In Fig. 2, the pulse energy as a function of time demonstrates that significant absorption of the 23 nC

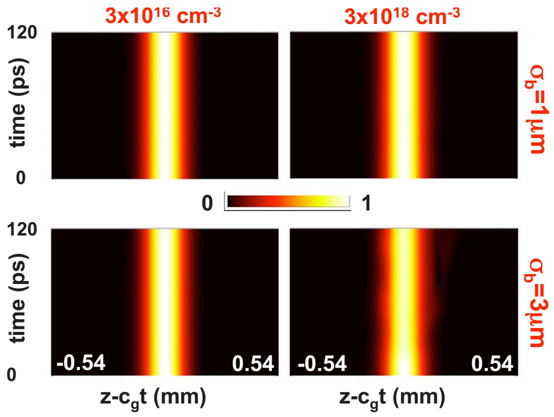

FIG. 1. (Color online) The evolution of the longitudinal pulse envelope over 120 ps for two different electron-beam densities char: 3×10^{16} and 3×10^{18} cm^{-3} and two different beam widths $\sigma_b=1$ μm and $\sigma_b=3$ μm.

pulse has occurred by 20 ps. A simple scaling for the time scale over which pump depletion occurs can be obtained by approximating the sum in Eq. (40) by

$$\sum_{part.} \vec{\xi}^*(r_i,z_i)\vec{v}_i(t)e^{-ik_0z_i} \approx 2N_b\left(\frac{m_ec^2}{q}\right)w_{ch}^{-1}J_1(\psi)a_0, \qquad (41)$$

which assumes all the electrons are properly phased for acceleration and near the peak of radial profile of the axial field. The scaling for the depletion time is then

$$\frac{\tau_d}{T_0} \sim \frac{a_0}{16\pi}J_1^{-1}(\psi)(k_0w_{ch})^3\left(\frac{L_b}{r_e}\right)N_b^{-1}, \qquad (42)$$

where T_0 is the laser period, $r_e=q^2/m_ec$ is the classical electron radius, L_b is the beam length, and N_b is the number of beam electrons. For a 23 nC beam, Eq. (42) gives $\tau_d=90$ ps, close to value found in the simulation, $0.3J(1-t/\tau_d)\sim0.23J$. After 20 ps, the beam moves into a lower amplitude section of the pulse and is no longer within the separatrix of the laser field. The beam and pulse then exchange energy in a cyclic manner. For higher beam charges, which may make the space-charge approximations marginal, the beam and pulse can undergo significant energy exchange, with the pulse losing almost all of its energy in certain axial regions and regaining it later in other axial regions. Because the depletion time scales inversely with the number of beam electrons, currently realizable beam charges, ~1 nC, are far from causing pump depletion in currently realizable waveguide limited durations, ~135 ps (4 cm).

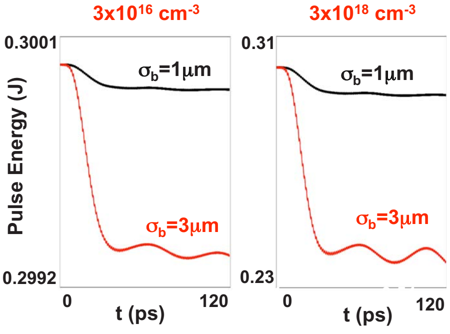

FIG. 2. (Color online) Evolution of pulse energy for all four electron beams considered.

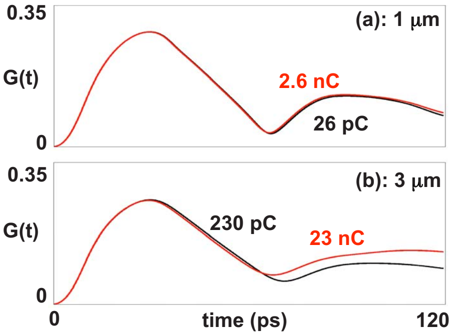

FIG. 3. (Color online) Bunching parameter as a function of time over 120 ps. In Figs. 3(a) and 3(b), $\sigma_b=1$ μm and $\sigma_b=3$ μm, respectively.

From Ref. [13], the condition for space-charge forces to overcome the axial accelerating field is given as

$$n_b[\text{cm}^{-3}] < \frac{3.6\times10^{12}}{[1+\lambda_p^2/\pi^2w_{ch}^2]}\delta a_o(w_{ch}\lambda_o)^{-1}[\text{cm}^{-2}], \qquad (43)$$

which for parameters considered here is $n_{b,0}<6.3\times10^{18}$ cm^{-3}. This density is greater than the densities considered here. We can then conclude that for the beams considered here, space-charge limitations on the electron beam will become important before pump depletion of the laser pulse. However, because pump depletion scales with the number of electrons in the beam and not the beam density, pump depletion may become important before space charge for large beam widths. For example, at $n_{b,0}=3.2\times10^{17}$ cm^{-3}, $\sigma_b=10$ μm gives ~8 nC and a $\sigma_b=30$ μm gives ~80 nC.

Although our simulations of the $n_{b,0}=3.0\times10^{18}$ cm^{-3} beam are close to the space-charge threshold for the beam widths considered, Eq. (43) overestimates the effect of space charge. Equation (43) assumes that the electrons have bunched into δ-function slabs axially, but the actual density is not so localized. To examine the axial localization of the electron beam, we define the bunching parameter

$$G(t) \equiv \left|\frac{1}{N_b}\sum_{i=1}^{N_b} e^{ik_0z_i(t)}\right|^2. \qquad (44)$$

When $G(t)=1$, the electron density can be considered axially periodic δ-function slabs where Eq. (43) holds; when $G(t)=0$, the electrons are uniformly distributed axially and the axial space-charge force for a long beam becomes negligible. Figures 3(a) and 3(b) show $G(t)$ for the 1 and 3 μm beams, respectively. The maximum for both beams is $G(t)\sim0.3$; Eq. (43) provides a conservative estimate on the axial space-charge limitation of the beam. The importance of radial space-charge effects was already discussed in Sec. II.

From Fig. 2, we see that the electron beam stops gaining energy before 120 ps; the rest of our results will examine effects occurring at 60 ps, half the pulse length dephasing

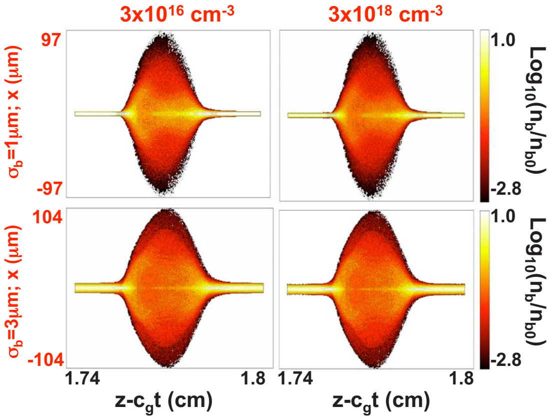

FIG. 4. (Color online) The log of the beam density normalized to the initial on-axis beam density after 60 ps. The vertical axis is transverse position and the horizontal axis is laser frame coordinate.

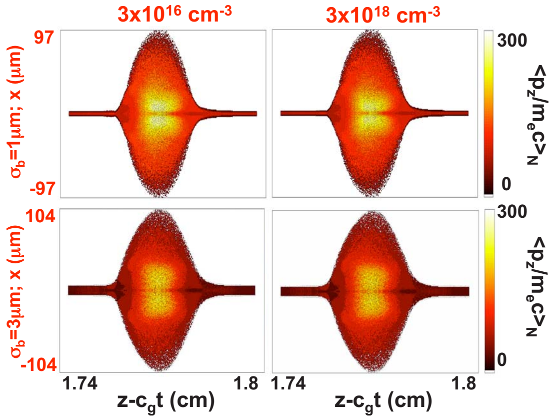

FIG. 6. (Color online) The number averaged axial momentum after 60 ps. The vertical axis is transverse position and the horizontal axis is laser frame coordinate.

time. Figure 4 depicts the log of the number averaged axial beam density for the 1 and 3 μm beams normalized to the initial on-axis density at the three different beam charges. The normalized densities are plotted as a function of final transverse and axial position in the laser frame coordinate, $z-c_g t$. For the 1 μm beam, there is not much change in the density as the charge is increased from 26 pC to 2.6 nC. The 3 μm beam follows the same trend as the 1 μm as the charge is increased. The 3 μm beam, however, has much less density on axis. The reduction in on-axis density occurs due to two effects of electrons initiated at larger radii: a larger quasi-phase-matched focusing/defocusing force and the reduced axial field at larger radii. The large quasi-phase-matched defocusing overcomes the increased ponderomotive focusing from the $m=0$ spatial harmonic for larger radii.

In addition, both the 1 and 3 μm beams display a charge piling behind and in front of the pulse. Figure 5 shows the on-axis normalized density profile for the 230 pC, 3 μm beam in solid. The pulse shape is also plotted as a reference. As demonstrated in Appendix C, the charge piling is not the result of the axial ponderomotive force of the pulse from the $m=0$. The charge piling is actually the result of the focusing force of the laser. In our previous work [13], we derived the time scale for focusing and defocusing of the beam due to the laser field

$$\tau \sim \left(\frac{2\pi}{\omega_0}\right)\gamma^{5/3}\left[\frac{(k_0 w_{ch})(k_0\lambda_p)(k_m\lambda_p)}{4\pi^5\delta a_0}\right]^{1/3}. \tag{45}$$

For the parameters considered here and using $a_0(z-c_g t)$ corresponding to where the charge piling occurs, we find $\tau \sim 50$ ps. As time increases, we expect to see the charge piling move along the axis away from the peak of the pulse.

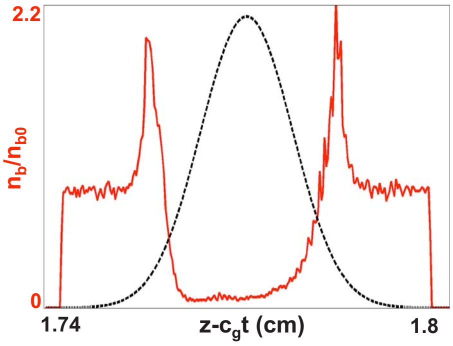

FIG. 5. (Color online) On-axis beam density as a function of beam frame coordinate normalized to the initial on-axis density for the 230 pC, 3 μm beam. The pulse shape is also plotted (dotted line) for reference.

As the beam charge is increased, the electron beam becomes axially modulated. We note that these modulations are insensitive to numerical parameters (i.e., spatiotemporal step size and particle number). Furthermore, the modulation wavelengths are not consistent with any other longitudinal scale in the problem and are too short to be explained by linear instability. The origin of the modulations is a secular growth of a density perturbation at the left and right edges of the electron beam. This effect is discussed in detail in Appendix D.

Figure 6 shows the number averaged momentum of the 1 and 3 μm electron beams after traveling 1.8 cm, half the pulse length dephasing distance. The axial momentum remains well confined on axis for both the 1 and 3 μm electron beams. As discussed previously, the low energy beam electrons scatter to large radii. The 3 μm beam has a larger transverse spread in momentum than the 1 μm beam. More of the properly phased electrons in the 3 μm beam sit at larger radii and experience a larger transverse quasi-phase-matched force. Half of the accelerating phase is initially defocused and the 3 μm beam acquires a larger transverse momentum spread. The maximum in the average momentum is similar for all four cases, suggesting that the electron beam gains most of its energy in the first 20 ps as demonstrated by Fig. 2.

Comparisons of the 1 and 3 μm electron beams at $n_e = 3\times 10^{18}$ cm^{-3} are depicted as the solid and dotted lines, respectively, in Fig. 7. The transversely averaged momentum as a function of axial distance is displayed in Fig. 7(a). The high-energy component of the beam is centered about the peak of the laser pulse. The average energy is higher and more concentrated axially for the 1 μm beam. Figure 7(b) shows the axially averaged axial momentum as a function of

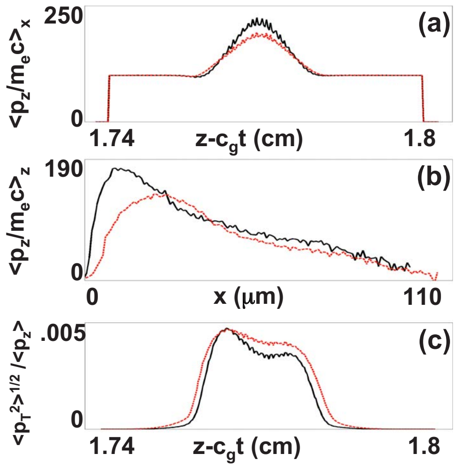

FIG. 7. (Color online) Comparison of the 1 and 3 μm electron beams at $n_e = 3\times 10^{18}$ cm^{-3}; the solid and dotted lines, respectively. (a) The transverse averaged axial momentum as a function of laser frame coordinate. (b) The axial averaged axial momentum as a function of transverse coordinate. (c) The beam divergence as a function of laser frame coordinate.

transverse coordinate. The axial momentum of the 1 μm beam is larger and stays more confined on axis. The beam divergence is plotted in Fig. 7(c). As expected, the 1 μm beam divergence is lower. The divergence is also slightly higher for both beams behind the peak of the laser pulse. Comparing to Fig. 7(a), we see that this is due to an increase in the transverse momentum and not a decrease in the axial momentum. One explanation for the asymmetry can be explained by a slight difference in the pulse amplitude for electrons starting to the left and right of the peak of the pulse. In particular, for a particle starting at z_0, where distance is measured from the peak of the pulse,

$$\eta(z,t) = \exp\left[-\left(\frac{|\delta k|}{k_0}ct + z_0\right)^2 (c\sigma_t)^{-2}\right]. \tag{46}$$

From Eq. (46), we see that $\eta(z_0>0,t) < \eta(z_0<0,t)$, thus the quasi-phase-matched defocusing force is larger for electrons starting behind the pulse than for those starting in front.

VI. PULSE AMPLIFICATION

As an inverse process to acceleration, it is possible to amplify the laser pulse via the deacceleration of electrons in the laser's field. To demonstrate this, we consider a periodic prebunched electron beam with a δ function radial profile

$$J_{b,z}(r,z) \cong qc\pi\sigma_b^2\lambda_o n_{b,o}\sum_{\ell=-L}^{L}\frac{\delta^2(r)\,\delta(z - v_{z,0}t - \ell\lambda_o)}{2\pi r}. \tag{47}$$

Upon inserting Eq. (47) into Eq. (10), we have the following expression for η:

$$\frac{\partial\eta}{\partial\tau} = -\alpha\frac{c}{w_{ch}}\sum_m i^m J_m(\psi)\left[1 + \sum_{\ell=1}^{\infty} 2\cos[k_0\ell(\Psi - \delta v\tau)]\right] \times e^{-i(k_o+mk_m+\delta k)\Psi - imc_gk_m\tau}, \tag{48}$$

where $\alpha = 2a_0^{-1}(\omega_{p,b}/\omega)^2(\sigma_b/w_{ch})^2$, $\delta v = v_{z0} - c_g$, and we have switched to the pulse frame coordinate with $\Psi = z - c_gt$ and $\tau = t$. Equation (48) also assumes the beam is long compared to the pulse length. Integrating over τ yields

$$\eta = -\alpha\frac{c}{w_{ch}}\sum_n i^{n+1}J_n(\psi)\left[\frac{1}{nc_gk_m} + \sum_{\ell=1}^{\infty}\frac{e^{\pm ik_0\ell(\Psi - \Delta v\tau)}}{nc_gk_m \mp \ell\,\delta vk_0}\right] \times e^{-i(k_o+nk_m+\delta k)\Psi - inc_gk_m\tau} + \eta(\Psi,0). \tag{49}$$

When the resonance condition, $mc_gk_m \mp \ell\Delta vk_0 = 0$, is satisfied, secular growth of the laser pulse occurs. The resonance condition provides the initial velocity that will maximize the pulse amplification. In particular, if we want to utilize the large relative amplitude of the $m=1$ spatial harmonic (the $m=0$ cannot be resonant), we have that $m=\ell$ and $v_{z0} = v_{p,1}$ where $v_{p,1}$ is the phase velocity of the $m=1$ harmonic. Invoking the resonance condition and dropping nonresonant terms, we find

$$\eta = 2\alpha\tau\frac{c}{w_{ch}}\sum_{m=1} i^m J_m(\psi)\exp\left(-i\left[\frac{k_0}{2\gamma_0^2} + (m-1)k_m\right]\Psi\right) + \eta(\Psi,0). \tag{50}$$

The $m=1$ spatial harmonic is essentially constant over the entire pulse frame coordinate, $\lambda = 2\gamma_0^2\lambda_0 \sim 1.6$ cm, and the amplitude of the other harmonics drops rapidly with increasing n. The time constant for secular growth of the pulse is then $\tau_{amp} \cong \tau_d$, where τ_d is given by Eq. (42). This is expected as our calculation for the depletion time assumed all the electrons were in the accelerating phase as opposed to the deaccelerating phase.

We note that τ_{amp} depends on the number of beam electrons, but is independent of the electron energy, a consequence of our assumption that the beam velocity was constant. In actuality, as the electrons slow down, the resonance condition acquires a velocity detuning that begins to limit the energy gain of the pulse. Higher energy electrons can transfer more energy to the pulse before velocity detuning becomes appreciable (γ depends sensitively on v at relativistic energies).

With current technology, it is much easier to create high-energy short laser pulses than it is to create bunched high-energy electron beams—one of the motivations of laser-plasma accelerators. Even if a high-energy, high-density electron beam could be created (perhaps from ultrahigh intensity laser–solid interactions), a second laser with $\lambda \sim 1/4\lambda_0$ would be required to bunch the electron beam before injection. Furthermore, our space-charge limitation for bunched beams, Eq. (43), limits the number of electrons that can be placed in the large deaccelerating region of the field. To overcome this limitation, one could imagine coaccelerating electrons and protons (or even positrons) in alternating half phases, but again this is far beyond current capabilities. We thus stipulate that our analysis and simulations of

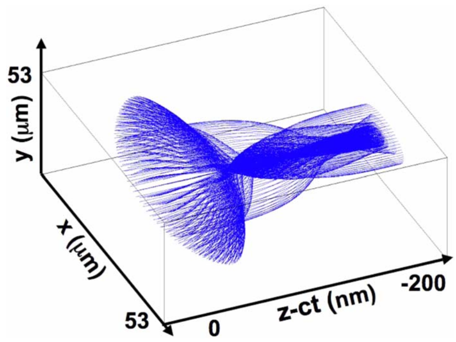

FIG. 8. (Color online) Quarter wavelength electron bunch after 120 ps as a function of transverse coordinate and beam frame coordinate. The beam is traveling from right to left and each point is one simulation particle.

pulse amplification are meant as a demonstration of a principle and not as a proposal of an application.

Here we consider an injected electron beam with 2.1 nC at 1 GeV: a total beam energy of 2.1 J. The electrons are distributed uniformly into $1/4\lambda_0$ long bunches with each bunch spaced by λ_0. The beam extends axially from −8 to 8 μm about the peak of the pulse and distributed as a Gaussian radially with a width of 9 μm. If the beams were uniform, the density would be $n_{b,0}=3.2\times 10^{18}$ cm^{-3}, close to our space-charge limitation; the initial localization parameter for the beam is $G(t)=0.9$. The laser and channel parameters are the same as the simulations presented in the previous section; the total initial laser energy is 300 mJ. We consider propagation over 120 ps (twice the time of the simulations in the previous section) or ~3.6 cm.

To provide intuition into the structure of the beam, we plot one electron bunch as a function of transverse coordinate and axial distance after 120 ps in Fig. 8 (one dot is one simulation electron). Figure 9(a) shows the initial longitudinal pulse shape (dotted line) and the pulse shape after 120 ps; the pulse has acquired energy from the electron beam. In Fig. 9(b), the pulse energy (dashed) and beam energy (dotted) are plotted as a function of time on the left axis. The pulse almost doubles in energy. The initial energy gain of the pulse grows linearly as predicted by Eq. (50). After ~40 ps, the energy gain slows down as the beam begins to outrun the pulse, moving into the lower amplitude region of the pulse. The right axis of Fig. 9(b) depicts the pulse width as a function of time. The pulse gets initially shorter due to amplification only where the beam overlaps the pulse. The pulse length begins to go up again after ~40 ps due to the beam beginning to amplify in the initially small amplitude region of the pulse.

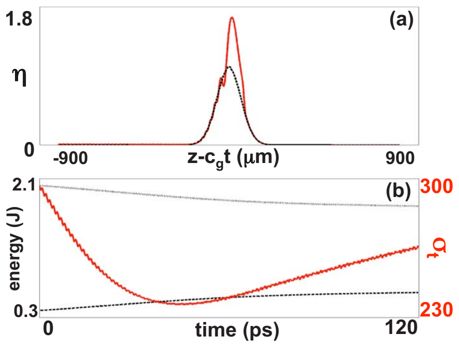

FIG. 9. (Color online) (a) Initial longitudinal pulse shape and pulse shape after 120 ps (the dotted and solid lines, respectively) as a function of laser frame coordinate. (b) The beam energy (dotted) and pulse energy (dashed) on the left axis. The pulse width (solid) is plotted on the right axis.

VII. SUMMARY AND CONCLUSIONS

As previously demonstrated [13], the corrugated plasma channel allows for the guiding of modes composed of slow wave spatial harmonics that can be phase matched to relativistic electron beams. Here we have analyzed and simulated the self-consistent interaction of a short-pulse laser and relativistic electron beam in a corrugated plasma channel. The effect of beam loading on the laser pulse and beam evolution was captured by separating the evolution of the pulse's phase and transverse profile from the evolution of the longitudinal envelope. The background plasma determines the laser's phase, whereas the longitudinal pulse profile evolved in response to the presence of the electron beam. The background plasma was chosen to model experimental density profiles [15], while also providing an analytic solution for the guided mode's phase. The laser and plasma parameters were chosen in correspondence with current experiments and the electron-beam parameters were varied.

A linear dispersion relation was derived for the longitudinal pulse profile in the presence of an electron-beam phase matched to the $m=1$ spatial harmonic of the guided mode. The electron beam considered was infinite in axial extent with an arbitrary radial profile. The dispersion relation included the effects of both the longitudinal and transverse motions of the electron beam in the laser field. Observing that the dispersion relation should reduce to an electrostatic beam dispersion relation in the absence of the laser field allowed for inclusion of space-charge effects. The electron beams considered were narrow with respect to the field profile and were analyzed in the O-type bunching limit of the dispersion relation. For the parameters considered, the electron beam was on the boundary of the strong and weak space-charge limits, but in both cases the instability growth lengths were shown to be much longer than currently existing plasma waveguides. The beam instabilities may be important, however, for smaller field amplitudes or higher beam densities and energies.

To simulate the self-consistent beam-pulse interaction, the phase of the laser due to the background plasma, which is independent of time, was calculated initially. The evolution of the longitudinal pulse shape and the equations of motion of the beam electrons, which determined the beam current, were iterated in time. By utilizing the transverse enveloping of the electromagnetic field, simulation particles were only interpolated onto an axial grid. This property allowed for a savings in both simulation time and noise.

We considered two beam widths, 1 and 3 μm, and two beam densities, 3×10^{16} and 3×10^{18} cm^{-3}. Depletion of the laser pulse was only significant for the 3 μm beam at

3×10^{18} cm^{-3}. As expected, the depletion occurs only while the beam overlaps the pulse. There was essentially no difference in the beam quality when the density was changed. We then concluded that over current wave-guided length limited times, ~60 ps, space-charge effects should become important before pulse depletion for the beams considered. However, because the time scale for pump depletion scales with the number of electrons and not the beam density, pump depletion may become more important for wider beams at similar densities.

The simulations also revealed two phenomena of the beam-pulse interaction: piling of the beam charge and axial asymmetry of the beam divergence. The charge piling was a result of laser focusing field pushing electrons inward. Because the time scale of this process is inversely proportional to the field amplitude, electrons starting at a larger axial distance from the peak of the pulse converge on axis at different times. This process sets up a charge pile on axes both trailing and leading the pulse. The axial asymmetry of the beam divergence arises from the relative motions of the electron beam and laser pulse, which produce an axial asymmetry in the quasi-phase-matched focusing-defocusing force.

We have also demonstrated that a properly phased electron beam can transfer energy to the pulse as an inverse process to acceleration. Because the energy transfer takes places locally (wherever the electron beam is), the shape of the resulting pulse is sensitive to where the electron beam starts and to the velocity mismatch between the beam and the group velocity of the laser. Charge and energy limitations on currently achievable electron beams make this phenomenon unfeasible for applications.

ACKNOWLEDGMENTS

The authors would like to acknowledge support from the DOE and NSF. In addition, the authors would like to thank A. G. York, H. M. Milchberg, P. Michel, B. Pollock, D. Froula, and L. Divol for fruitful conversations. J.P.P. would also like to thank the Institute for Research in Electrical and Applied Physics at the University of Maryland where a large portion of this research was conducted.

APPENDIX A: SEPARATION OF PROPAGATION EQUATIONS

To demonstrate the separability of Eqs. (6) and (10) for ξ and η, respectively, we start with the generalized electromagnetic wave equations

$$\nabla\times\nabla\times\vec{E}+\frac{1}{c^2}\frac{\partial^2}{\partial t^2}\vec{E}=-\frac{4\pi}{c^2}\left(\frac{\partial\vec{J}_p}{\partial t}+\frac{\partial\vec{J}_b}{\partial t}\right),\qquad\text{(A1)}$$

$$\nabla\times\nabla\times\vec{B}+\frac{1}{c^2}\frac{\partial^2}{\partial t^2}\vec{B}=\frac{4\pi}{c}\nabla\times(\vec{J}_p+\vec{J}_b),\qquad\text{(A2)}$$

where $\vec{J}_p$ and $\vec{J}_b$ are the background plasma and electron-beam currents, respectively. Upon inserting Eqs. (4) and (5) into Eqs. (A1) and (A2), respectively, we find

$$\eta D_1\vec{F}+\frac{\partial\eta}{\partial z}D_2\vec{F}-\frac{\partial\eta}{\partial t}\left(\frac{2ik_0}{c}\right)\vec{F}=-\frac{4\pi}{c^2}e^{-i\Phi}\times\left[\frac{\partial}{\partial t}-i\omega-c(\nabla+ik_0\hat{z})\times\right]\vec{J}_b,\qquad\text{(A3)}$$

where all the spatiotemporal derivatives are now slow derivatives ($d/dz\ll k_0$ and $d/dt\ll\omega$), we have defined $\vec{F}\equiv(\xi_r,\beta_\theta,\xi_z)$, the D_i are given by

$$D_1=(\nabla+ik_0\hat{z})\times(\nabla\times\,)-ik_0\left(\frac{\partial}{\partial z}+\frac{i}{c}\frac{\omega_p^2}{\omega}-ik_0\hat{z}\hat{z}\cdot-\hat{z}\nabla\cdot\right),\qquad\text{(A4)}$$

$$D_2=\hat{z}\times(\nabla\times\,)-\left(\frac{\partial}{\partial z}+2ik_0-2ik_0\hat{z}\hat{z}\cdot-\hat{z}\nabla\cdot\right),\qquad\text{(A5)}$$

and we have defined $\Phi\equiv(k_0z-\omega t)$. Thus far, we have only assumed that the background plasma responds linearly and nonrelativistically to the laser electric field (this is consistent with our parameters of interest, $qE_0/\omega m_ec\sim0.25$) and we have dropped higher-order derivatives of z and t which may contribute to group-velocity dispersion over long propagation distances, $\sim w_{ch}^4/\lambda_0^3$. Taking the vector component of Eq. (A4), we obtain the following:

$$\hat{r}\cdot D_1\vec{\xi}=-\left[\nabla_r^2-\frac{1}{r^2}+2ik_0\frac{\partial}{\partial z}-\frac{\omega_p^2}{c^2}\right]\xi_r+\frac{\partial}{\partial r}\nabla\cdot\vec{\xi}+ik_0\frac{\partial}{\partial r}\xi_z,\qquad\text{(A6)}$$

$$\hat{z}\cdot D_1\vec{\xi}=-\left[\nabla_r^2+k_0^2+ik_0\frac{\partial}{\partial z}-\frac{\omega_p^2}{c^2}\right]\xi_z+\left[ik_0+\frac{\partial}{\partial z}\right]\nabla\cdot\vec{\xi},\qquad\text{(A7)}$$

$$\hat{\theta}\cdot D_1\beta\hat{\theta}=-\left[\nabla_r^2-\frac{1}{r^2}+2ik_0\frac{\partial}{\partial z}-\frac{\omega_p^2}{c^2}\right]\beta.\qquad\text{(A8)}$$

Using the fact that ω and k_0 provide the fastest time and space scales, respectively, we can write

$$\nabla\cdot\vec{\xi}=-\frac{\nabla\varepsilon}{\varepsilon}\cdot\vec{\xi}-ik_0\xi_z+\left(\frac{4\pi q}{\varepsilon\eta}\right)e^{-i\Phi}n_b.\qquad\text{(A9)}$$

Plugging Eq. (A9) into Eqs. (A5) and (A6), keeping terms to lowest order in ω_p^2/ω^2, we have

$$\hat{r}\cdot D_1\vec{\xi}=-\left[\nabla_r^2-\frac{1}{r^2}+2ik_0\frac{\partial}{\partial z}-\frac{\omega_p^2}{c^2}\right]\xi_r+\left(\frac{4\pi q}{\eta}\right)e^{-i\Phi}\frac{\partial n_b}{\partial r},\qquad\text{(A10)}$$

$$\hat{z}\cdot D_1\vec{\xi}=-\left[\nabla_r^2+2ik_0\frac{\partial}{\partial z}-\frac{\omega_p^2}{c^2}\right]\xi_z+\left(\frac{4\pi q}{\eta}\right)\left(ik_0+\frac{\partial}{\partial z}\right)e^{-i\Phi}n_b.\qquad\text{(A11)}$$

We can find similar expressions for components of D_2 as follows:

$$\hat{r}\cdot D_2\vec{\xi}=\frac{\partial}{\partial r}\xi_z-2\left[ik_0+\frac{\partial}{\partial z}\right]\xi_r, \tag{A12}$$

$$\hat{z}\cdot D_2\vec{\xi}=\nabla\cdot(\hat{r}\xi_r), \tag{A13}$$

$$\hat{\theta}\cdot D_2\beta\hat{\theta}=-2\left[ik_0+\frac{\partial}{\partial z}\right]\beta, \tag{A14}$$

and we note that D_2 includes off diagonal terms that couple the three-field components.

Rewriting Eq. (A3) we have that

$$\eta\vec{\vec{W}}\vec{F}+\frac{\partial\eta}{\partial z}D_2\vec{F}-\frac{\partial\eta}{\partial t}\left(\frac{2ik_0}{c}\right)\vec{F}=-\frac{4\pi}{c^2}e^{-i\Phi}$$
$$\times[\Lambda\vec{J}_b+qc^2(\nabla+ik_0\hat{z})n_b], \tag{A15}$$

where we have defined

$$\Lambda\equiv\frac{\partial}{\partial t}-i\omega-c[(\nabla+ik_0\hat{z})\times],$$

and the tensor $\vec{\vec{W}}$ has diagonal elements given by the coefficients of ξ_r, ξ_z, and β on the right-hand side of Eqs. (A6)–(A8), respectively. We now divide Eq. (A15) by η, multiply by $\vec{F}^*$, subtract the conjugate of Eq. (A15), multiplied by $\vec{F}$, and integrate over the transverse area. The resulting coefficients are

$$\int[\vec{\xi}^*\vec{\vec{W}}\vec{\xi}+\beta^*D_3\beta-\text{c.c.}]d^2r=0 \tag{A16}$$

$$\int[\vec{\xi}^*D_2\vec{\xi}+\beta^*D_2\beta]d^2r\cong-2ik_0\int(\beta^*\xi_r+\beta\xi_r^*)d^2r, \tag{A17}$$

$$\frac{2ik_0}{c}\int(|\vec{\xi}|^2+|\beta|^2)d^2r=4ik_0U, \tag{A18}$$

where we have used $\omega_p^2/\omega^2\ll 1$, $d/dz\ll k_0$, and U is the electromagnetic field energy. From Eq. (A17), we have the following:

$$-2ik_0\int(\beta^*\xi_r+\beta\xi_r^*)d^2r=-4ik_0P. \tag{A19}$$

Noting that $c/c_g=U/P$ [23] and defining $\aleph\equiv(\partial/\partial z+c_g^{-1}\partial/\partial t)$, we have

$$\aleph\eta=-i\frac{\pi}{\omega cP}\int e^{-i\Phi}\vec{F}^*\cdot[\Lambda\vec{J}_b+qc^2(\nabla+ik_0\hat{z})n_b]d^2r. \tag{A20}$$

Using the fact that $d/dz\ll k_0$ and $d/dt\ll\omega$ and keeping lowest-order terms, we find

$$\Lambda\vec{J}_b+qc^2(\nabla+ik_0\hat{z})n_b\cong-2i\omega J_r\hat{r}+c(\hat{\theta}+\hat{r})\frac{\partial}{\partial r}J_z. \tag{A21}$$

Upon integrating $\beta_\theta^*\partial J_z/\partial r$ by parts and using $\beta_\theta^*\cong\xi_r^*$ and $\nabla\cdot(\hat{r}\xi_r^*)\cong ik_0\xi_z^*$,

$$\Lambda\vec{J}_b+qc^2(\nabla+ik_0\hat{z})n_b\cong-2i\omega[J_r\hat{r}+J_z\hat{z}], \tag{A22}$$

where the equality only holds under the integral in Eq. (A20). Finally, we arrive at the equation describing the evolution of the longitudinal pulse shape in the presence of a relativistic beam current

$$\left[\frac{\partial}{\partial z}+\frac{1}{c_g}\frac{\partial}{\partial t}\right]\eta=-\frac{2\pi}{cP}\int e^{-i(k_0z-\omega t)}\vec{\xi}^*\cdot\vec{J}_bd^2r. \tag{A23}$$

The longitudinal evolution, Eq. (A23), has been separated from the phase and transverse evolution of the electromagnetic field, $\vec{\vec{W}}\vec{\xi}=0$.

In arriving at Eq. (A23), we have assumed that $\omega_p^2/\omega^2\ll 1$, $qE_0/\omega m_ec<1$, $d/dz\ll k_0$, and $d/dt\ll\omega$. All of these inequalities are well satisfied in our parameter region of interest. Whereas the first two conditions are typically satisfied for laser-based accelerators, future studies may require relaxation of the requirement on the field amplitude, necessitating a more rigorous treatment of the plasma current. Because the energy gain in quasi-phase-matched acceleration scales linearly with the pulse length, pulses on the order of laser period are not of interest here. Other applications may require these pulse durations and cannot be modeled under the assumptions made here.

APPENDIX B: DISCUSSION OF SINGLE RADIAL MODE ASSUMPTION

To consider coupling of multiple radial eigenmodes through the beam current, we start with the generalized radial electric field in the plasma channel

$$E_r(r,z,t)=\sum_{\ell,odd}2^{-\ell}\eta_\ell(z,t)H_\ell(r/w_{ch})e^{-r^2/w_{ch}^2+i\Phi_\ell(z,t)}, \tag{B1}$$

where $\Phi_\ell(z.t)=(k_0+\delta k_\ell)z+\psi\cos(k_mz)-\omega t$ and $\delta k_\ell=-(\omega_p^2/2\omega^2+4\ell/k_0^2w_{ch}^2)$.

The multimode generalization of Eq. (10) can then be written as

$$\left[\frac{\partial}{\partial z}+\frac{1}{c_{g,\ell}}\frac{\partial}{\partial t}\right]\eta_\ell=-\frac{2\pi}{cP_\ell}\int e^{-i(k_0z-\omega t)}\vec{\xi}_\ell^*\cdot\vec{J}_bd^2r, \tag{B2}$$

where $c_{g,\ell}=c(1-\omega_p^2/2\omega^2-4\ell/k_0^2w_{ch}^2)$ and P_ℓ are the generalized group velocity and power, respectively, and the orthogonality property of the radial functions has been used. The beam current coupling allows transfer of energy between the radial modes; the electromagnetic forces from all modes determine the electron's velocity. The radial profile of the electron beam changes in response to the laser field. If the projection of the beam's radial profile onto the radial profile of a

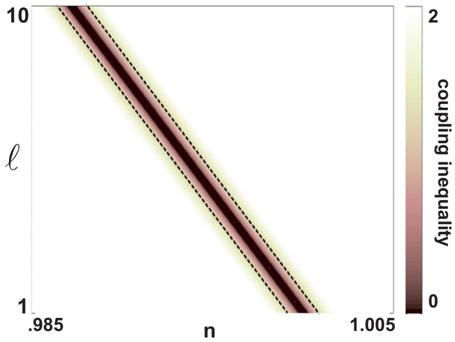

FIG. 10. (Color online) Coupling inequality from the left-hand side of Eq. (B4) as a function of radial eigenmode number, ℓ, and spatial harmonic number, n. Between the dotted lines, the inequality is less than 1.

given eigenmode becomes significant, the beam can deplete or pump this mode, depending on the phase of the contributing electrons.

For an incident laser pulse, where the incident radial profile is well approximated by the lowest radial eigenmode of the channel, very little of the energy will be contained in the higher-order eigenmodes. For 100% coupling efficiency to the plasma channel, the relative amplitudes of the waveguide modes can be determined from

$$\xi_\ell = \frac{1}{\pi 2^{\ell+1}} \int E_{i,r}(r) H_\ell(r/w_{ch}) e^{-r^2/w_{ch}^2} d^2 r, \qquad \text{(B3)}$$

where $E_{i,r}(r)$ is the incident radial profile of the laser. If $\xi_1 \gg \xi_{\ell \neq 1}$, the contribution of the modes with $\ell > 1$ can be neglected altogether.

Even if $\xi_1 \gg \xi_{\ell \neq 1}$ is marginally satisfied, the beam current coupling to the $\ell > 1$ will be weak due the rapidly varying phase of these modes in the beam frame. The contribution of electrons based on their phase can be determined by considering the initial phase matching conditions. If the initial phase velocity of the $(m,\ell)=(1,1)$ spatial harmonic is set to c $(\delta k_1 + k_m = 0)$ and we know that this mode responds strongly to an electron beam with $v_{z0} = c(1 - 1/2\gamma_0^2)$, the condition for weaker response can be written as

$$\gamma_0^2 \left| \frac{\omega_p^2}{\omega^2}(m-1) - \frac{8}{(k_0 w_{ch})^2}(m-\ell) \right| \geq 1. \qquad \text{(B4)}$$

For modes that satisfy the above inequality, the energy will typically oscillate between the beam and the mode, but no long-time net energy transfer would occur. The left-hand side of Eq. (B4) is plotted in Fig. 10 for the parameters used here. The color contour has been maxed out at 2 due to the rapid increase of the function in both m and ℓ. The dotted lines represent equality with 1 and between the dotted lines is where the phase of the (m,ℓ) mode allows for strong coupling with the electron beam. The plot shows that our condition for weak coupling is violated only for $(m,\ell)=(1,1)$ (the mode that couples to the electron beam by design). As γ increases from the initial value, the coupling to other modes should be further reduced. Furthermore higher-order radial eigenmodes will fall behind the electron beam at a faster rate due to their decreased group velocity. We note that in other situations, Eq. (B4) may be satisfied for a finite number of (m,ℓ) pairs. In this situation, the beam can be a source of Raman instability for the pulse, but this is a topic for future research.

APPENDIX C: PONDEROMOTIVE PILING

We can show that the charge piling is not the result of the axial ponderomotive force of the pulse from the $m=0$ spatial harmonic. For small radii, the axial ponderomotive force is

$$F_z^{pm} = -\frac{m_e c^2}{\gamma_0}\left(\frac{2a_0}{k_0 w_{ch}}\right)^2 \left[1 - \frac{4}{\pi^2}\frac{v_0}{c}\left(\frac{\lambda_p}{w_{ch}}\right)^2 \times \left(1 + \frac{2\lambda_p^2}{\pi^2 w_{ch}^2}\right)^{-1}\right]^2 \hat{z} \cdot \nabla e^{-2(z - c_g t/c\sigma_t)^2}. \qquad \text{(C1)}$$

If we expand the above equation about the maximum $(z = c_g t + c\sigma_t/2)$ and set $z = v_{z0} t + z_1$, we have, to lowest order,

$$\frac{d^2 z_1}{dt^2} = \frac{4\alpha e^{-1/2}}{m_e c \sigma_t \gamma_0^3}\left[1 - \left(\frac{2}{c\sigma_t}\right)^2 \left(z_1 + \frac{\delta k}{k_0} ct - \frac{c\sigma_t}{2}\right)^2\right], \qquad \text{(C2)}$$

where α is the magnitude of the coefficient of the gradient in Eq. (C1). Because we are interested in $z_1 \approx c\sigma_t/2$, we can solve Eq. (C2) iteratively and find for $t < \tau \equiv \sigma_t e^{1/4}(m_e c^2 \gamma_0^3/4\alpha)^{1/2}$,

$$z_1 \cong z_{1,0} - \frac{\delta k}{k_0} ct + \frac{c\sigma_t}{2}\left(\frac{t}{\tau}\right)^2 \left[1 - \left(\frac{2 z_{1,0}}{c\sigma_t} - 1\right)^2\right]. \qquad \text{(C3)}$$

We can now show that any two charges initially separated by any distance for $z_1 > c\sigma_t/2$ will get closer in space and thus cause a piling of charge. From Eq. (C3), we have that

$$\frac{z_1^B(t) - z_1^A(t)}{z_{1,0}^B - z_{1,0}^A} \cong 1 - 2\left(\frac{t}{\tau}\right)^2 \left(\frac{z_{1,0}^B + z_{1,0}^A}{c\sigma_t} - 1\right). \qquad \text{(C4)}$$

Noting that $z_{1,0}^B + z_{1,0}^A \geq c\sigma_t$ for two charges starting to the right of maximum, the separation always decreases for $t < \tau$. Electrons in the strong region of the ponderomotive force are able to catch up with those in the weaker region of the force resulting in a local axial focusing of the beam. The time scale for this process to occur can be estimated from τ, which for our parameters are $\tau \sim 50$ ns, a much longer time scale than those considered here.

APPENDIX D: MODULATIONS OF THE ELECTRON BEAM

The modulations of the electron beam are an edge effect due to the finite extent of the electron beam. To demonstrate this, we start by considering the beam dynamics at the beam boundary. For simplicity, we limit our analysis to the longitudinal dynamics. The electromagnetic field is treated as a perturbation on the beam, which is justified because the beam boundary is at $\sigma_B = 3.3 c\sigma_t$ of the laser pulse. A zeroth order beam profile $n_0(z) = n_0[1 - \Theta(z - v_{z0}t - \sigma_B)]$, where Θ is the unit step function and a zeroth order velocity $u_{z,0}(z)$

$=v_{z0}$ satisfies a simple fluid equilibrium. We now perturb this equilibrium with the presence of the $m=1$ spatial harmonic. The first-order equations are then

$$\frac{\partial n_1}{\partial \tau} + \frac{\partial}{\partial \zeta}(v_1 n_0) = 0, \tag{D1}$$

$$\frac{\partial v_1}{\partial \tau} = 2\frac{a_0 J_1(\psi)}{\gamma_0^3}\left(\frac{c^2}{w_{ch}}\right)\eta(\zeta,\tau)e^{ik(\zeta-\Delta v\,\tau)} + \text{c.c.}, \tag{D2}$$

where we have switched to the beam frame coordinates and defined $\Delta v \equiv c - v_{z0}$. Differentiating Eq. (D1) and noting that n_0 is independent of τ, we find

$$\frac{\partial^2 n_1}{\partial \tau^2} = -\alpha e^{ik(\zeta-\Delta v\,\tau)}\eta\frac{\partial}{\partial \zeta}n_0 + \text{c.c.}, \tag{D3}$$

where $\alpha = 2a_0 J_1(\psi)c^2/w_{ch}\gamma_0^3$ and we have used the fact that the density derivative across the beam boundary is large. Integrating twice over τ and using the condition that $n_1(\tau=0)=0$ yields the following:

$$n_1(\zeta,\tau) \cong -\tau\frac{\alpha b n_0}{k\Delta v}\frac{\zeta - ib}{\zeta^2 + b^2}e^{-(\zeta/c\sigma_t)^2 + ik\zeta}\delta(\zeta - \sigma_B) + \text{c.c.}, \tag{D4}$$

where $b = k(c\sigma_t)^2(\Delta v/\delta v)$, $\delta v = c - c_g$, and we note that Eq. (D4) is only valid for $\tau < 4\gamma_0^2/\omega_0 \sim 17$ ps. The perturbation of the electric field across the beam edge produces an impulse perturbation in the density that grows secularly in the beam frame. We iterate to find the effect of n_1 on η by inserting Eq. (D4) into Eq. (10) with $J_b \cong qcn_1$. Switching to pulse frame coordinates and defining the pulse frame coordinate $\Psi \equiv z - c_g t$, we have the following:

$$\frac{1}{c}\frac{\partial \eta_1}{\partial \tau} \cong \frac{32}{\gamma_0}\frac{J_1(\psi)}{(k_0 w_{ch})^2}\left(\frac{\omega_{p,b}}{\omega_0}\right)^2\left(\frac{\sigma_b}{w_{ch}}\right)^2 \times e^{-11}(\omega_0\tau)\delta(\Psi - \tau\delta v - \sigma_B), \tag{D5}$$

where we have dropped the phase and note that the strongest response will be when the phase is an integer multiple of 2π. Upon integrating, we obtain the response of the pulse from the secular growth of the beam perturbation

$$\eta_1 = \frac{32}{\gamma_0}\frac{J_1(\psi)}{(k_0 w_{ch})^2}\left(\frac{\omega_{p,b}}{\omega_m}\right)^2\left(\frac{\sigma_b}{w_{ch}}\right)^2 \times e^{-11}[k(\Psi - \sigma_B)][\Theta(\Psi - \sigma_B - \tau\delta v) - \Theta(\Psi - \sigma_B)]. \tag{D6}$$

The first-order density leaves an imprint on the laser pulse that grows in spatial extent and size as the electron beam moves through the pulse for $\Psi > \sigma_B$. Because the imprint on the pulse is initially small in spatial extent, it is very broad spectrally and is able to drive short-wavelength modulations of the electron beam. Figure 11, a zoomed in version of Fig. 1 for the 3 μm, 37 nC beam at $\Psi \sim \sigma_B$, shows the growth of this imprint in our simulations. From Eq. (D6), we obtain the following effective growth time for the imprint perturbation:

$$\tau_{imp} = \frac{e^{11}}{32}\frac{\gamma_0}{J_1(\psi)}\left(\frac{\omega_m}{\omega_{p,b}}\right)^2\left(\frac{w_{ch}}{\sigma_b}\right)^2(k_0 w_{ch})^2\omega_0^{-1}, \tag{D7}$$

which, for the parameters considered here, gives $\tau_{imp} \sim 3.4$ ns. This is close to the size of the perturbation shown in Fig. 11 for small times $\eta_1(\tau=2.5\text{ ps}, \Psi=\sigma_B) \cong 6\times10^{-4}$ from the simulation and our growth time gives $2.5/3400 \cong 7\times10^{-4}$. Because the field at $\Psi=\sigma_B$ is initially small, the field enhancement from the imprint quickly surpasses the initial field in amplitude, which results in a feedback; the nonlinearity causes the imprint and field amplitude to grow quickly as seen in Fig. 11 (our simple model in this appendix only works for $t \ll \tau_{imp}$). We note that smoothing the axial beam boundaries could eliminate this effect, while higher-density beams would exasperate the effect.

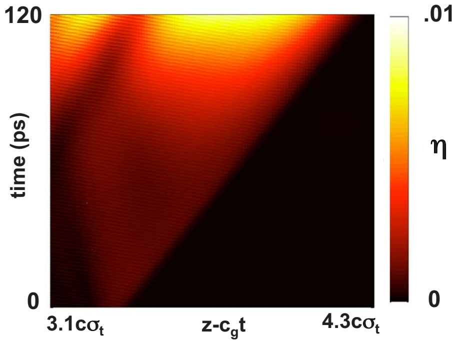

FIG. 11. (Color online) Secular growth of a perturbation in the pulse and the corresponding imprint due to the rigid beam boundary as a function of laser frame coordinate (horizontal axis) and time (vertical axis).

[1] J. D. Lindl *et al.*, Phys. Plasmas **11**, 339 (2004).

[2] O. L. Landen, D. R. Farley, S. G. Glendinning, L. M. Logory, P. M. Bell, J. A. Koch, F. D. Lee, D. K. Bradley, D. H. Kalantar, C. A. Back, and R. E. Turner, Rev. Sci. Instrum. **72**, 627 (2001).

[3] H. Tabak, J. Hammer, M. E. Glinsky, W. L. Kruer, S. C. Wilks, J. Woodworth, E. M. Campbell, and M. D. Perry, Phys. Plasmas **1**, 1626 (1994).

[4] J. Fuchs, P. Antici, E. d'Humières, E. Lefebvre, M. Borghesi, E. Brambrink, C. A. Cecchetti, M. Kaluza, V. Malka, M. Manclossi, S. Meyroneinc, P. Mora, J. Schreiber, T. Toncian, H. Pépin, and P. Audebert, Nat. Phys. **2**, 48 (2006).

[5] I. Spencer, K. W. D. Ledingham, R. P. Singhal, T. McCanny, P. McKenna, E. L. Clark, K. Krushelnick, M. Zepf, F. N. Beg, M. Tatarakis, A. E. Dangor, P. A. Norreys, R. J. Clarke, R. M. Allott, and I. N. Ross, Nucl. Instrum. Methods Phys. Res. B **183**, 449 (2001).

[6] T. Tajima and J. M. Dawson, Phys. Rev. Lett. **43**, 267 (1979).

[7] W. P. Leemans, B. Nagler, A. J. Gonsalves, Cs. Toth, K. Nakamura, C. G. R. Geddes, E. Esarey, C. B. Shroeder, and S. M. Hooker, Nat. Phys. **2**, 696 (2006).
[8] D. H. Froula, L. Divol, P. Davis, J. P. Palastro, P. Michel, V. Leurent, S. H. Glenzer, B. Pollock, and G. Tynan, Plasma Phys. Control. Fusion **51**, 024009 (2009).
[9] P. Sprangle, E. Esarey, and J. Krall, Phys. Plasmas **3**, 2183 (1996).
[10] T. Plettner, R. L. Byer, E. Colby, B. Cowan, C. M. S. Sears, J. E. Spencer, and R. H. Siemann, Phys. Rev. Lett. **95**, 134801 (2005).
[11] W. D. Kimura, G. H. Kim, R. D. Romea, L. C. Steinhauer, I. V. Pogorelsky, K. P. Kusche, R. C. Fernow, X. Wang, and Y. Liu, Phys. Rev. Lett. **74**, 546 (1995).
[12] P. Serafim, P. Sprangle, and B. Hafizi, IEEE Trans. Plasma Sci. **28**, 1190 (2000).
[13] J. P. Palastro, T. M. Antonsen, S. Morshed, A. G. York, and H. M. Milchberg, Phys. Rev. E **77**, 036405 (2008).
[14] A. G. York, H. M. Milchberg, J. P. Palastro, and T. M. Antonsen, Phys. Rev. Lett. **100**, 195001 (2008).
[15] B. D. Layer, A. York, T. M. Antonsen, S. Varma, Y.-H. Chen, and H. M. Milchberg, Phys. Rev. Lett. **99**, 035001 (2007).
[16] J. H. Cooley, T. M. Antonsen, H. M. Milchberg, J. Fan, L. Margolin, and L. Pyatnitskii, Phys. Rev. E **73**, 036404 (2006).
[17] *Modern Microwave and Millimeter-Wave Power Electronics*, edited by R. J. Barker, N. C. Luhmann, J. H. Booske, and G. S. Nusinovich (Wiley-IEEE Press, New York, 2005), ISBN: 978-0-471-68372-8.
[18] G. M. Branch and T. G. Mihran, IRE Trans. Electron Devices **2**, 3 (1955).
[19] J. R. Pierce, *Traveling Wave Tubes* (D. Van Nostrand and Co., New York, 1950).
[20] J. J. Su, T. Katsouleas, J. M. Dawson, P. Chen, M. Jones, and R. Keinigs, IEEE Trans. Plasma Sci. **15**, 192 (1987).
[21] R. D. Ruth, A. W. Chao, P. L. Morton, and P. B. Wilson, Part. Accel. **17**, 171 (1985).
[22] P. Chen, Part. Accel. **20**, 171 (1986).
[23] J. D. Jackson, *Classical Electrodynamics* (John Wiley & Sons, Inc., New York, 1962).